Journal of Materials Chemistry A

ROYAL SOCIETY OF CHEMISTRY

PAPER

View Article Online
View Journal

Cite this: DOI: 10.1039/d5ta10123a

Lithium coordination disorder controlling ionic conductivity in mixed-halide borate glasses

Yohei Onodera, *[a] Yasuyuki Takimoto,[b] Hiroyuki Hijiya,[c] Noriyoshi Kayaba,[c] Masamichi Tanida,[d] Kazutaka Ikeda [e] and Shinji Kohara [a]

Understanding the structure–property relationships in glasses remains challenging owing to their structural complexity, especially in multicomponent practical glasses. In this work, neutron diffraction with isotopic substitution was employed to investigate lithium coordination environments in halide (chloride and/or bromide)-doped borate glasses, which exhibit variations in lithium-ion conductivity associated with anion mixing. Lithium-specific neutron pair distribution function analysis reveals that the conductivity enhancement in oxide–halide mixed glasses originates from the breaking of one short Li–O bond and the formation of two longer Li–halogen bonds. The formation of LiO_3Cl_2 and LiO_3Br_2 units is observed in chloride- and bromide-doped glasses, respectively, whereas a glass containing equal amounts of chloride and bromide exhibits LiO_3ClBr units in addition to LiO_3Cl_2 and LiO_3Br_2 units. These results suggest that the coexistence of multiple lithium–oxygen–halogen polyhedral units hinders lithium-ion migration, leading to reduced ionic conductivity in halide–halide mixed glasses. This work provides new insights into the structure–property relationships in lithium-ion conducting glasses through lithium-specific structural analysis.

Received 11th December 2025
Accepted 23rd March 2026

DOI: 10.1039/d5ta10123a

rsc.li/materials-a

1. Introduction

Glasses with high ionic conductivity have attracted considerable attention since the discovery of superionic conducting glasses by Minami and coworkers in 1977.[1,2] In recent years, there has been an increase in research focusing on the practical utilization of ionic conducting glasses as solid electrolytes for lithium-ion batteries, particularly for portable devices and electric vehicles.[3,4] The substitution of a flammable organic electrolyte in conventional lithium-ion batteries with a solid electrolyte has the potential to enhance battery safety and improve energy and power densities. Consequently, candidate materials must exhibit high ionic conductivity when utilized as solid electrolytes. A comprehensive understanding of lithium-ion conduction mechanisms in solid electrolytes is essential for the development of new materials with high ionic conductivity. The mechanism of lithium-ion conduction in crystalline ionic conductors has been elucidated through crystal structure analysis,[5,6] which has accelerated materials development. In contrast, the absence of long-range order in glasses makes analytical approaches developed for crystalline materials inapplicable. Therefore, structural studies of glasses require a combination of techniques, including diffraction, spectroscopy, and computer simulations, to elucidate the mechanism underlying ionic conductivity.

Numerous studies have been conducted on ionic conducting oxide and sulfide glasses to date. In oxide glasses, borate-[7] and phosphate-[8] based glasses are known to exhibit lithium-ion conductivity. Recently, ternary lithium borovanadate (Li_2O–V_2O_5–B_2O_3) glasses have been reported to exhibit an ionic conductivity of the order of 10^{-4} S cm^{-1} at room temperature, representing the highest level of ionic conductivity among oxide glasses.[9] Structural studies have shown that lithium incorporation significantly modifies the glass network. For example, ^{10}B nuclear magnetic resonance (NMR) spectroscopy revealed that the structural units in binary Li_2O–B_2O_3 glasses transform from boroxol, diborate, and tetraborate units to metaborate, pyroborate, orthoborate, and loose BO_4 tetrahedral units with increasing Li_2O content, creating non-bridging oxygens.[10] An increase in the number of non-bridging oxygens with increasing Li_2O content has also been observed in Li_2O–V_2O_5–B_2O_3 glasses.[9] Similar depolymerization of the network consisting of PO_4 tetrahedra has also been observed in Li_2O–P_2O_5 glasses based on ^{31}P magic angle spinning (MAS) NMR measurements.[11] On the other hand, X-ray and neutron diffraction studies demonstrated that lithium ions are tetrahedrally

[a]Center for Basic Research on Materials, National Institute for Materials Science, Sengen 1-2-1, Tsukuba, Ibaraki 305-0047, Japan. E-mail: ONODERA.Yohei@nims.go.jp
[b]Innovative Technology Laboratories, AGC, Inc., 1-1 Suehiro-cho, Tsurumi-ku, Yokohama, Kanagawa 230-0045, Japan
[c]Materials Integration Laboratories, AGC, Inc., 1-1 Suehiro-cho, Tsurumi-ku, Yokohama, Kanagawa 230-0045, Japan
[d]Electronic Materials General Division, Electronics Company, AGC Inc., 1-5-1 Marunouchi, Chiyoda-Ku, Tokyo 100-8405, Japan
[e]Neutron Industrial Application Promotion Center, Comprehensive Research Organization for Science and Society, 162-1 Shirakata, Tokai, Naka, Ibaraki 319-1106, Japan

coordinated by four oxygen atoms in borate and phosphate glasses.[12–14] Moreover, ionic conduction pathways in these glasses have been visualized using bond valence (BV) analysis of structure models generated by reverse Monte Carlo (RMC) modelling based on diffraction data.[15–18] In sulfide glasses, the development of $Li_7P_3S_{11}$ glass ceramic obtained by partial crystallization of $70Li_2S$–$30P_2S_5$ glass, which exhibits an ionic conductivity exceeding 10^{-3} S cm^{-1} comparable to that of organic liquid electrolytes, has significantly stimulated research in the Li_2S–P_2S_5 system.[19] Spectroscopic studies using Raman[19] and ^{31}P MAS NMR[20,21] techniques revealed that the fundamental structural units in $70Li_2S$–$30P_2S_5$ glass and $Li_7P_3S_{11}$ glass ceramic are thiophosphate species such as $P_2S_7^{4-}$ and PS_4^{3-}. Structural analyses combining diffraction experiments and RMC modelling have indicated that fourfold coordination around lithium ions plays an important role in ionic conduction[22] and have enabled visualization of conduction pathways[23] through BV analysis.[15–18] Recent studies combining RMC modelling and first-principles calculations have further clarified the structural and dynamical features associated with lithium-ion migration in Li_2S–P_2S_5 glasses.[24–26]

Consequently, lithium-ion-conducting glasses have been extensively investigated in response to growing interest in all-solid-state lithium-ion batteries. However, the intricate interplay between the lithium coordination environment and the conduction mechanism in glasses remains incompletely understood. Understanding this relationship is crucial for the rational design of glassy solid electrolytes with improved ionic conductivity. Beyond studies focused directly on ionic conduction, it is well recognized that the physical and functional properties of multicomponent glasses can be systematically tuned through compositional variation. Variations in cation and anion species have been shown to modify optical, dielectric, and mechanical properties in a variety of multicomponent oxide glasses, including rare-earth-doped lead–silicate[27] and lead–borate[28] glasses, lithium fluoroborophosphate glasses,[29] CuO-doped silicate[30] and aluminosilicate[31] glasses, and halide-substituted borophosphate glasses.[32] These findings highlight that compositional diversity strongly influences both local structures and macroscopic properties in glasses. In particular, glasses containing mixed anions have attracted attention because combining different anion species can significantly influence ionic conductivity.[33,34] Nevertheless, only a limited number of structural studies have been reported for such mixed-anion glasses.

One major challenge arises from the difficulty of extracting lithium-related structural information from the disordered atomic arrangements of multicomponent glasses, even when neutron diffraction, which is sensitive to light elements, is employed. Lithium exhibits a negative neutron coherent scattering length ($b = -1.90$ fm),[35] and atomic correlations between lithium and other atoms appear as negative peaks in the pair distribution function (PDF) obtained by neutron diffraction. However, in multicomponent glasses, these negative peaks often overlap with other positive peaks, making quantitative structural analysis extremely difficult. Therefore, an element-specific experimental approach is required to determine the lithium coordination environment and to clarify its role in ionic conduction.

In this study, we investigated five compositions of $1/3Li_2O$–$1/3B_2O_3$–$1/3LiCl_{1-x}Br_x$ glasses, in which single Cl, single Br, and mixtures of Cl and Br in the ratios of 1 : 3, 1 : 1, and 3 : 1 were adopted. To clarify the effect of the addition and mixing of halide anions on ionic conductivity, the structures of the glasses were examined using a combination of high-energy X-ray and neutron diffraction measurements. Specifically, in this study, we employed the neutron diffraction with isotopic substitution (NDIS) technique[36–38] to investigate lithium-specific atomic correlations. The NDIS technique utilizes the difference in neutron coherent scattering lengths between isotopes and allows us to obtain element-specific structural information. Indeed, structural studies with a particular focus on lithium using NDIS have been reported for Li_2O–$2SiO_2$,[39] Li_2O–$2B_2O_3$,[40] and $LiAlSiO_4$ glasses.[41] In this study, two glasses with different lithium isotopic enrichments were prepared, enabling lithium-specific structural data to be obtained from the difference between neutron diffraction data. Consequently, the interatomic distances and coordination numbers around lithium cations were determined by lithium-specific PDF analysis employing the NDIS data. The coordination numbers for non-lithium-related correlations were also determined using neutron diffraction data of ^{null}Li-enriched glasses, where the coherent neutron scattering length of lithium is adjusted to zero. In addition, the structural parameters obtained were verified through their application to the reproduction of high-energy X-ray diffraction data. Thus, a cutting-edge structural analysis, founded upon element-specific quantum beam measurements, has been meticulously executed. In this work, we investigate the relationship between the lithium coordination environments and ionic conductivity in $1/3Li_2O$–$1/3B_2O_3$–$1/3LiCl_{1-x}Br_x$ glasses using lithium-specific structural information obtained by our novel structural analysis.

2. Experimental

2.1 Preparation of glasses

The $1/3Li_2O$–$1/3B_2O_3$–$1/3LiCl_{1-x}Br_x$ ($x = 0$, 0.25, 0.5, 0.75, and 1) glasses were prepared from mixtures of reagent-grade Li_2CO_3, $H_3{}^{11}BO_3$, LiCl, and LiBr. The mixtures were melted at 900–1000 °C for 15 min, and each melt was then quenched by the twin-roller method. In this study, two types of glasses with different lithium isotope ratios were prepared: ^{nat}Li-enriched $1/3Li_2O$–$1/3B_2O_3$–$1/3LiCl_{1-x}Br_x$ glasses (^{nat}Li glasses) and ^{null}Li-enriched $1/3Li_2O$–$1/3B_2O_3$–$1/3LiCl_{1-x}Br_x$ glasses (^{null}Li glasses). For the preparation of the ^{null}Li glasses, a mixture of $^{nat}Li_2CO_3$ and $^6Li_2CO_3$ was used to achieve the ^{null}Li composition (^{6}Li : ^{7}Li = 0.5265 : 0.4735). For comparison, the $0.5Li_2O$–$0.5B_2O_3$ ($LiBO_2$) glass was also prepared in a similar manner to the $1/3Li_2O$–$1/3B_2O_3$–$1/3LiCl_{1-x}Br_x$ glasses. The densities of the glasses were measured by helium gas pycnometry using a AccuPyc II 1340 gas pycnometer (Micrometrics, USA).

2.2 Conductivity measurements

The electrical conductivities of the $1/3Li_2O$–$1/3B_2O_3$–$1/3LiCl_{1-x}Br_x$ glasses were measured at room temperature by the

ac four-probe method using a Solartron SI 1287 frequency response analyser (Solartron Analytical, UK). Au electrodes with a diameter of 4 mm were formed on both sides of the glass-flake samples by vacuum deposition. The applied voltage was 50 mV, and the frequency range was from 1 Hz to 1 MHz. All measurements were carried out under a dry-air atmosphere. The electrical conductivities of the glasses were determined from the resistance values obtained at the real-axis intercept of the Nyquist plots.

2.3 NMR measurements

^{11}B MAS NMR experiments were conducted on the $1/3Li_2O$–$1/3B_2O_3$–$1/3LiCl_{1-x}Br_x$ glass samples at room temperature using an ECA600 spectrometer (JEOL, Japan). The experiments were conducted with a ^{11}B Larmor frequency of 192.55 MHz with a spin rate of 20 kHz and a pulse delay of 3 s. The ^{11}B chemical shifts were estimated with respect to an external saturated boric acid solution (19.6 ppm). The obtained spectra were subsequently deconvoluted into two components.

2.4 Diffraction measurements

The high-energy X-ray diffraction experiments were conducted at beamline BL04B2 at SPring-8 (Hyogo, Japan) using a diffractometer dedicated to disordered materials.[42] Crushed glass samples were loaded into SiO_2 glass capillaries. The incident X-ray energy was 61.23 keV. The diffraction patterns of the glasses were measured at room temperature in transmission geometry. The intensity of the incident X-rays was monitored in an Ar-filled ionization chamber, and the scattered X-rays were detected using four CdTe detectors and three Ge detectors. A vacuum chamber was used to suppress air scattering around the sample. The raw data were corrected for polarization, absorption, and background, and the contribution of Compton scattering was subtracted using standard data analysis software.[43]

The neutron diffraction measurements were conducted on the high-intensity total diffractometer, NOVA,[44] installed at beamline BL21 of the Materials and Life Science Experimental Facility (MLF) at the J-PARC spallation neutron source (Ibaraki, Japan). The crushed glass samples were loaded into vanadium–nickel (V–Ni) null alloy cells with an outer diameter of 6.0 mm and a thickness of 0.1 mm. The wavelength range of the incident neutron beam was $0.12 < \lambda < 8.3$ Å. Measurements were performed for the samples contained in the V–Ni cell, the empty V–Ni cell, the empty instrument, and a vanadium standard for normalization at room temperature. The observed scattering intensities for the samples were corrected for the instrument background and for attenuation by the sample and cell. Subsequently, the corrected intensities were normalized using the incident beam profile and further corrected for multiple and incoherent scattering.

The fully corrected X-ray and neutron diffraction data were normalized to give the Faber–Ziman total structure factor $S(Q)$:[45]

$$S(Q) = 1 + \frac{1}{|\langle W(Q)\rangle|^2}\sum_{\alpha=1}^{n}\sum_{\beta=1}^{n} c_\alpha c_\beta w_\alpha(Q) w_\beta(Q)[S_{\alpha\beta}(Q) - 1], \quad (1)$$

where c_α is the atomic fraction of chemical species α and $w_\alpha(Q)$ represents either a Q-dependent atomic scattering (form) factor $[f_\alpha(Q)]$ with a dispersion term in X-ray diffraction or a Q-independent coherent scattering length (b_α) in neutron diffraction. $S_{\alpha\beta}(Q)$ is the partial structure factor for the chemical species α and β, and

$$\langle W(Q)\rangle = \sum_{\alpha=1}^{n} c_\alpha w_\alpha(Q). \quad (2)$$

Total correlation functions, $T(r)$, were obtained by a Fourier transform of $S(Q)$ with a Lorch function, $M(Q)$.[46]

$$T(r) = 4\pi r\rho + \frac{2}{\pi}\int_{Q_{\min}}^{Q_{\max}} (S(Q) - 1)\sin(Qr)M(Q)\mathrm{d}Q \quad (3)$$

Here, ρ is the average number density.

To obtain lithium-specific structural information, the NDIS was employed. The NDIS technique allows element-specific structural information to be obtained by utilizing the difference in coherent neutron scattering lengths between isotopes. In the present study, two glasses with identical chemical compositions but different lithium isotopic ratios (^{nat}Li and ^{null}Li glasses) were prepared. Because only the neutron scattering length of lithium differs between the two samples, taking the difference between the diffraction data extract structural correlations involving lithium atoms. The differential intensity $\Delta_{Li}I(Q)$ between the scattering intensities of the ^{nat}Li and ^{null}Li glasses is expressed as

$$\Delta_{Li}I^{coh}(Q) = \Delta_{Li}[\langle b^2\rangle - \langle b\rangle^2] + \Delta_{Li}[\langle b^2\rangle]\Delta_{Li}S(Q), \quad (4)$$

and

$$\langle b\rangle^2 = \left(\sum_\alpha c_\alpha b_\alpha\right)^2, \quad (5)$$

$$\langle b\rangle^2 = \sum_\alpha c_\alpha {b_\alpha}^2, \quad (6)$$

where the term $\Delta_{Li}[\ ]$ denotes the difference between the values in the brackets for the ^{nat}Li and ^{null}Li glasses. The differential structure factor $\Delta_{Li}S(Q)$ can be expressed as a linear combination of the partial structure factors, $S_{\alpha\beta}(Q)$, as follows:

$$\Delta_{Li}S(Q) = \sum_{\alpha=1}^{n}\sum_{\beta=1}^{n}\Delta_{Li}w_{\alpha\beta}S_{\alpha\beta}(Q), \quad (7)$$

where the weighting factors $\Delta_{Li}w_{\alpha\beta}$ are given by

$$\Delta_{Li}w_{\alpha\beta} = c_\alpha c_\beta\frac{\Delta_{Li}[b_\alpha b_\beta]}{\Delta_{Li}\left[\langle b\rangle^2\right]}. \quad (8)$$

Compared with the total structure factors $S(Q)$ obtained from X-ray and neutron diffraction, $\Delta_{Li}S(Q)$ significantly enhances the contributions from Li-related $S_{\alpha\beta}(Q)$ while suppressing contributions from the other partials. Accordingly, $\Delta_{Li}S(Q)$ for the $1/3Li_2O$–$1/3B_2O_3$–$1/3LiCl_{1-x}Br_x$ glasses can be expressed as

$$\Delta_{Li}S(Q) = \Delta_{Li}w_{LiLi}S_{LiLi}(Q) + 2\Delta_{Li}w_{LiB}S_{LiB}(Q) + 2\Delta_{Li}w_{LiO}S_{LiO}(Q) + 2\Delta_{Li}w_{LiCl}S_{LiCl}(Q) + 2\Delta_{Li}w_{LiBr}S_{LiBr}(Q), \quad (9)$$

where the weighting factors for the partials other than those mentioned above were negligible; therefore, these partial structure factors were effectively eliminated in $\Delta_{Li}S(Q)$.

To obtain detailed structural information on the short range, $S(Q)$ and $T(r)$ were analysed using the pair function method proposed by Mozzi and Warren.[47] The pair function method is useful for analysing real-space functions from which the structural parameters such as the interatomic distance and coordination number can be determined. Utilizing the pair function formalism, the calculated total correlation function $T^{calc}(r)$ was obtained using the following equation for the interatomic distance $r_{\alpha-\beta}$ and coordination number $N_{\alpha-\beta}$ of the α–β pair:

$$T^{calc}_{\alpha-\beta}(r) = \frac{2}{\pi}\int_{Q_{min}}^{Q_{max}} \frac{2c_\alpha N_{\alpha-\beta} w_\alpha(Q) w_\beta(Q)}{\langle W(Q)\rangle^2} \exp\left(-\frac{1}{2}l_{\alpha-\beta}{}^2Q^2\right) \times \frac{\sin(\pi Q/Q_{max})}{\pi Q/Q_{max}} \frac{\sin(Qr_{\alpha-\beta})}{r_{\alpha-\beta}} \sin\, Qr\mathrm{d}Q. \quad (10)$$

The term $l_{\alpha-\beta}$ is a convergence factor representing the static and thermal disorders of the α–β correlation. The calculated differential total correlation function $\Delta_{Li}T^{calc}(r)$ was also obtained using the following equation for the interatomic distance $r_{Li-\beta}$ and coordination number $N_{Li-\beta}$ of the Li–β pair:

$$\Delta_{Li}T^{calc}_{Li-\beta}(r) = \frac{2}{\pi}\int_{Q_{min}}^{Q_{max}} \frac{2c_{Li}N_{Li-\beta}\Delta_{Li}[b_{Li}b_\beta]}{\Delta_{Li}\langle b\rangle^2} \exp\left(-\frac{1}{2}l_{Li-\beta}{}^2Q^2\right) \times \frac{\sin(\pi Q/Q_{max})}{\pi Q/Q_{max}} \frac{\sin(Qr_{Li-\beta})}{r_{Li-\beta}} \sin\, Qr\mathrm{d}Q. \quad (11)$$

The variations in $r_{\alpha-\beta}$ ($r_{Li-\beta}$) and $N_{\alpha-\beta}$ ($N_{Li-\beta}$) obtained from the fitting $T(r)$ and $\Delta_{Li}T(r)$ were estimated to be ±0.02 Å and ±0.3, respectively.

3. Results and discussion

3.1 Glass composition and density

The chemical compositions of the obtained $1/3Li_2O$–$1/3B_2O_3$–$1/3LiCl_{1-x}Br_x$ glasses are listed in Table 1. The glasses are designated by the ratio of Cl to Br, *e.g.*, Cl50Br50 refers to a glass containing an equal mixture of Cl and Br ($1/3Li_2O$–$1/3B_2O_3$–$1/3LiCl_{0.5}Br_{0.5}$ glass). The densities of the $1/3Li_2O$–$1/3B_2O_3$–$1/3LiCl_{1-x}Br_x$ glasses are summarized in Table 2. The density increases monotonically with the degree of Br substitution. The average number densities ρ of the $1/3Li_2O$–$1/3B_2O_3$–$1/3LiCl_{1-x}Br_x$ glasses, calculated from these densities, are also listed in Table 2.

Table 1 Compositions of glasses

	Element (at%)				
Glass sample	Li	B	O	Cl	Br
Br100	31.6	18.9	39.1	0	10.4
Cl25Br75	30.6	19.6	39.7	2.5	7.5
Cl50Br50	30.1	20.3	41.3	4.3	4.0
Cl75Br25	28.0	21.5	42.0	6.7	1.8
Cl100	29.4	20.5	40.8	9.3	0

Table 2 Mass density and atomic number density of glasses

Glass sample	Density (g cm^{-3})	Number density (Å^{-3})
Br100	2.47	0.0790
Cl25Br75	2.38	0.0817
Cl50Br50	2.28	0.0874
Cl75Br25	2.18	0.0884
Cl100	2.06	0.0880

3.2 Conductivity

The electrical conductivities of the $1/3Li_2O$–$1/3B_2O_3$–$1/3LiCl_{1-x}Br_x$ glasses range from 2.7×10^{-6} to 6.6×10^{-6} S cm^{-1} at room temperature (Fig. 1). These values are approximately one order of magnitude higher than those of $LiBO_2$ glass ($\sim 10^{-7}$ S cm^{-1}),[48–50] indicating that the addition of halide anions enhances the lithium-ion conductivity. Similar behaviour has been reported in other glass systems, including Li_2O–B_2O_3–LiX (X = F, Cl, Br, I),[7] $LiPO_3$–LiX (X = Cl, Br, I),[51] and Li_2S–B_2S_3–LiI.[52]

It is well established that the mixing of different types of anion, known as the mixed-anion effect, enhances lithium-ion conductivity in various glass systems.[33,34] Indeed, the $1/3Li_2O$–$1/3B_2O_3$–$1/3LiCl_{1-x}Br_x$ glasses exhibit enhanced conductivity in comparison with $LiBO_2$ glass, attributable to the mixing of oxide and halide anions. In contrast, the Cl25Br75, Cl50Br50, and Cl75Br25 glasses exhibit a substantial decrease in conductivity compared with the Cl100 and Br100 glasses, as shown in Fig. 1. In particular, the Cl50Br50 glass exhibits the lowest conductivity among the $1/3Li_2O$–$1/3B_2O_3$–$1/3LiCl_{1-x}Br_x$ glasses, suggesting that the mixing of halide anions leads to a reduction in conductivity. Therefore, the variation in ionic conductivity for the $1/3Li_2O$–$1/3B_2O_3$–$1/3LiCl_{1-x}Br_x$ glasses can be interpreted in

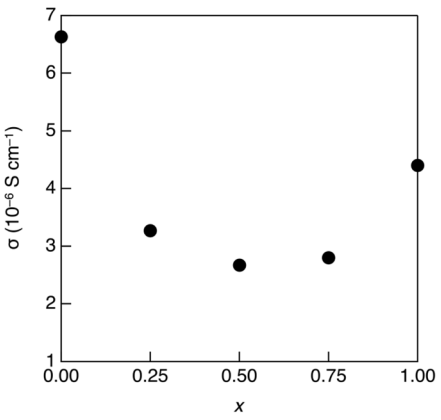

Fig. 1 Electrical conductivity of the $1/3Li_2O$–$1/3B_2O_3$–$1/3LiCl_{1-x}Br_x$ glasses.

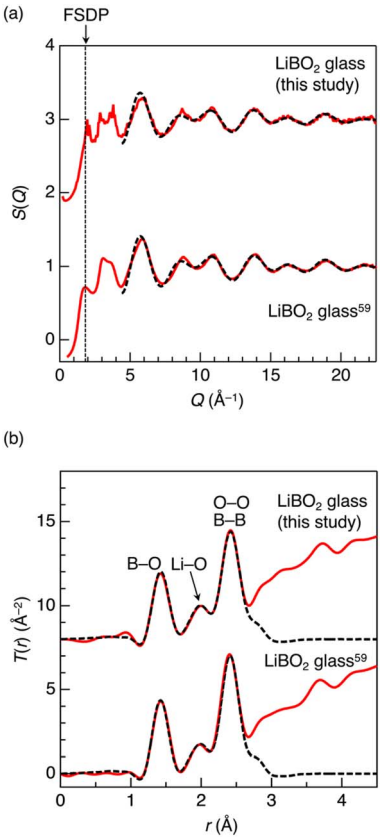

Fig. 2 X-ray diffraction data of $LiBO_2$ glasses in (a) Q space and (b) real space. Red solid curves represent experimental data, and black broken curves represent calculated data.

two stages: (i) enhancement of ionic conductivity induced by the mixing of oxide and halide anions, and (ii) reduction of ionic conductivity caused by the mixing of halide (chloride and bromide) anions. A comparable phenomenon is observed in silicate glasses exhibiting the mixed alkali effect, where alkali mixing leads to substantial reductions in conductivity, viscosity, and dielectric constant.[53–55] In our previous study, a combination of PDF analysis with structural modelling revealed that potassium ions were trapped within highly coordinated potassium–oxygen polyhedra, forming a correlated pair arrangement with sodium–oxygen polyhedra in a silicate glass with the mixed alkali effect.[55] Therefore, the variation in ionic conductivity shown in Fig. 1 is closely related to changes in the lithium coordination environment in the $1/3Li_2O$–$1/3B_2O_3$–$1/3LiCl_{1-x}Br_x$ glasses. To elucidate the structural origin of this behaviour, the local atomistic structure around lithium ions was examined by combining high-energy X-ray diffraction and NDIS.

3.3 Coordination number analyses using diffraction data

3.3.1 B_2O_3 glass. The ternary or quaternary $1/3Li_2O$–$1/3B_2O_3$–$1/3LiCl_{1-x}Br_x$ glasses contain structural information on 10 or 15 atomic pairs in the X-ray and neutron diffraction data. Prior to the structural analysis of these complicated glasses, we analyse the diffraction data of B_2O_3 (ref. 56) and $LiBO_2$ glasses. The B–O, O–O, and B–B coordination numbers in B_2O_3 glass, obtained using the pair function method based on neutron and X-ray $S(Q)$ and $T(r)$ (Fig. S1), are 3.0, 4.0, and 3.0, respectively. These results are consistent with the reported structure of B_2O_3 glass, in which trigonal planar BO_3 units form a network by sharing vertex oxygen atoms.[56–58]

3.3.2 $LiBO_2$ glass. Fig. 2(a) shows the X-ray $S(Q)$ for $LiBO_2$ glass prepared in this study together with previously reported data.[59] The $LiBO_2$ glass prepared in this study exhibits several Bragg peaks in $S(Q)$, indicating partial crystallization. In contrast, the behaviour of $S(Q)$ in the higher-Q region ($Q > 4.8$ Å^{-1}) is similar between the two $LiBO_2$ glasses. Compared with the X-ray $S(Q)$ of B_2O_3 glass (Fig. S1(a)), the first sharp diffraction peak (FSDP), a signature of intermediate-range order in the B–O covalent network,[56–58] shifts to higher Q values and becomes broader in both $LiBO_2$ glasses, indicating modification of the B–O covalent network upon lithium incorporation. The $T(r)$ functions obtained from the Fourier transform of $S(Q)$ are shown in Fig. 2(b). In addition to the B–O, O–O, and B–B correlations observed in B_2O_3 glass (Fig. S1(b)), a Li–O correlation peak appears at approximately 2.0 Å. Furthermore, the B–O peak shifts to a longer r and becomes asymmetric. The X-ray $S(Q)$ and $T(r)$ were analysed using the pair function method (eqn (10)). Two pair functions were used for each correlation to reproduce the asymmetric B–O and Li–O peaks. The calculated curves, shown as black broken lines in Fig. 2a and (b), reproduce the experimental $S(Q)$ and $T(r)$ well. The derived structural parameters are summarized in Table 3. The B–O peak in $T(r)$ was reproduced by two B–O pair functions at 1.42 and 1.63 Å. The B–O coordination numbers were 3.2 (this study) and 3.25 (previous diffraction data[59]), indicating the presence of BO_4 tetrahedral units, consistent with previous NMR and Raman spectroscopic studies.[10,50,60] The Li–O correlation peak was also reproduced by two pair functions at 1.98 and 2.35 Å, yielding a Li–O coordination number of 4.1. This suggests that lithium cations are tetrahedrally coordinated by oxygen atoms, with three shorter Li–O bonds at 1.98 Å and one longer interaction extending to approximately 2.35 Å. This configuration is consistent with a previous NDIS study on Li_2O–$2SiO_2$ glass.[39] The O–O distance (2.41–2.42 Å) and coordination number (4.4) are slightly larger than those in B_2O_3 glass (Table S1), reflecting the formation of BO_4 tetrahedral units. The B–B distance also increases slightly to 2.42 Å, suggesting an increase in the distance between the centres of neighbouring BO_x (BO_3 or

Table 3 Structural parameters for B–O, Li–O, O–O, B–B, and Li–B correlations in $LiBO_2$ glasses, derived from X-ray diffraction data

	B–O (I)		B–O (II)		Li–O (I)		Li–O (II)		O–O		B–B		Li–B	
	r_{B-O} (Å)	N_{B-O}	r_{B-O} (Å)	N_{B-O}	r_{Li-O} (Å)	N_{Li-O}	r_{Li-O} (Å)	N_{Li-O}	r_{O-O} (Å)	N_{O-O}	r_{B-B} (Å)	N_{B-B}	r_{Li-B} (Å)	N_{Li-B}
$LiBO_2$ glass (this study)	1.42	2.75	1.63	0.45	1.98	3.2	2.35	0.9	2.42	4.4	2.42	2.4	2.70	4.0
$LiBO_2$ glass[59]	1.42	3.00	1.63	0.25	1.98	2.9	2.35	1.2	2.41	4.4	2.42	2.4	2.70	4.0

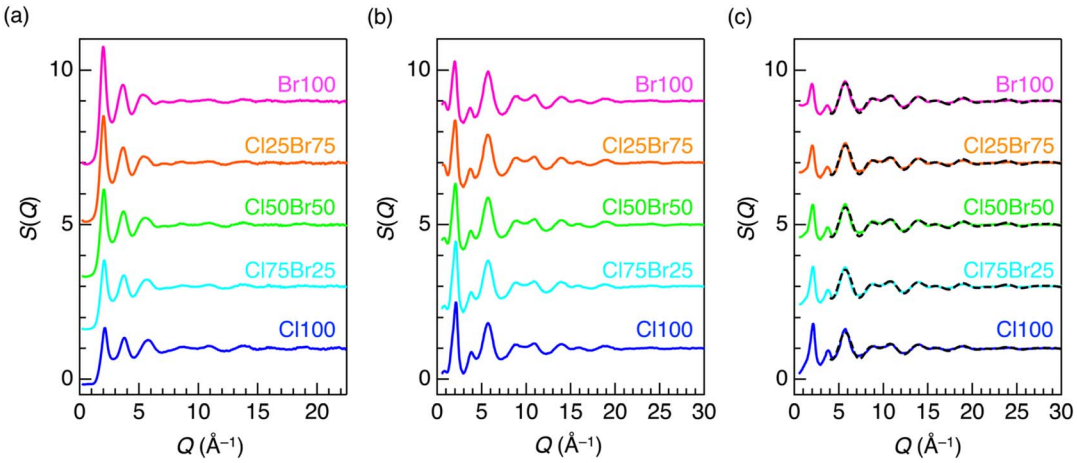

Fig. 3 X-ray and neutron diffraction data of the $1/3Li_2O–1/3B_2O_3–1/3LiCl_{1-x}Br_x$ glasses in Q space. (a) X-ray structure factors, (b) neutron structure factors of ^{nat}Li glasses, and (c) neutron structure factors of ^{null}Li glasses. Coloured solid curves represent experimental data, and black broken curves in panel (c) represent calculated data.

BO_4) units upon lithium incorporation. To examine the spatial relationship between lithium cations and BO_x units, a Li–B correlation was included in the pair function analysis. In $LiBO_2$ glass, Li_2O acts as a network modifier, converting bridging oxygens (B–O–B) into non-bridging oxygens, with Li^+ cations located nearby to maintain local charge neutrality.[61] The oxygen atoms introduced by Li_2O either form BO_4 units or exist as non-bridging oxygens. These oxygens are predominantly coordinated to lithium cations, giving rise to Li–O–B linkages. The resulting Li–B coordination number of approximately 4.0 is consistent with the Li–O coordination number (4.1), supporting this structural model. Based on the structural features identified for $LiBO_2$ glass, we proceed to analyse the structure of halide-containing $1/3Li_2O–1/3B_2O_3–1/3LiCl_{1-x}Br_x$ glasses.

3.3.3 $1/3Li_2O–1/3B_2O_3–1/3LiCl_{1-x}Br_x$ glasses. Fig. 3 shows the X-ray and neutron total structure factors, $S(Q)$, of the $1/3Li_2O–1/3B_2O_3–1/3LiCl_{1-x}Br_x$ glasses. The neutron $S(Q)$ exhibits different behaviours between the ^{nat}Li (Fig. 3(b)) and ^{null}Li (Fig. 3(c)) glasses, owing to the absence of Li-related weighting factors in the ^{null}Li glasses. The FSDP observed at $Q \sim 1.6$ Å^{-1}, which is prominent in B_2O_3 glass (Fig. S1(a)), is not clearly observed in either the X-ray or neutron $S(Q)$ for the $1/3Li_2O–1/3B_2O_3–1/3LiCl_{1-x}Br_x$ glasses due to the large weighting factors of chlorine and bromine for both X-rays and neutrons. The X-ray and neutron $T(r)$ functions, obtained from the Fourier transforms of $S(Q)$, are shown in Fig. 4. In the X-ray $T(r)$ data (Fig. 4(a)), the B–O and Li–O correlations exhibit small peaks at approximately 1.4 and 2.0 Å, respectively, in all the glasses. The peak observed at approximately 2.4 Å in all the glasses corresponds to overlapping O–O and B–B correlations. In the Cl100 glass, the Li–Cl correlation contributes to this peak, whereas in the Br100 glass, the Li–Br correlation appears at approximately 2.7 Å (as indicated by the arrow in Fig. 4(a)). In the neutron $T(r)$ for the ^{nat}Li glasses (Fig. 4(b)), B–O and Li–O peaks are clearly observed in all the glasses. The Li–O peak appears as a negative peak owing to the negative neutron coherent scattering length of ^{nat}Li ($b = -1.90$ fm).[35] Assignment of peaks beyond the B–O and Li–O correlations is difficult due to the overlap between

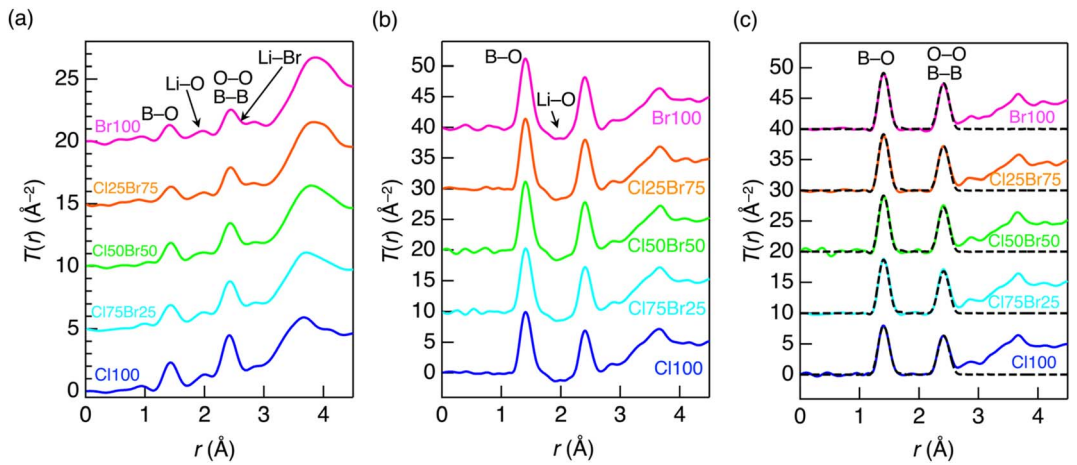

Fig. 4 X-ray and neutron diffraction data of the $1/3Li_2O–1/3B_2O_3–1/3LiCl_{1-x}Br_x$ glasses in real space. (a) X-ray total correlation functions, (b) neutron total correlation functions of ^{nat}Li glasses, and (c) neutron total correlation functions of ^{null}Li glasses. Coloured solid curves represent experimental data, and black broken curves in panel (c) represent calculated data.

Table 4 Structural parameters for B–O, O–O, and B–B correlations in the $1/3Li_2O$–$1/3B_2O_3$–$1/3LiCl_{1-x}Br_x$ glasses, derived from neutron diffraction data of ^{null}Li glasses

	B–O (I)		B–O (II)		O–O		B–B	
	r_{B-O} (Å)	N_{B-O}	r_{B-O} (Å)	N_{B-O}	r_{O-O} (Å)	N_{O-O}	r_{B-B} (Å)	N_{B-B}
Br100	1.40	3.0	1.52	0.4	2.41	4.0	2.42	2.4
Cl25Br75	1.40	3.0	1.52	0.4	2.41	4.0	2.42	2.4
Cl50Br50	1.40	3.0	1.52	0.4	2.41	4.0	2.41	2.4
Cl75Br25	1.40	3.0	1.52	0.4	2.41	4.0	2.42	2.4
Cl100	1.40	3.0	1.52	0.4	2.41	4.0	2.42	2.4

positive correlations (*e.g.*, O–O, B–B, and halogen–halogen peaks) and negative correlations (*e.g.*, Li–Cl, Li–Br, and Li–B peaks). In contrast, the ^{null}Li glasses (Fig. 4(c)) show the absence of Li–O peaks, while the B–O peaks remain, demonstrating the effective elimination of Li-related correlations. The second peak at 2.4 Å can therefore be assigned to overlapping O–O and B–B correlations. Notably, B–Cl and B–Br correlations, expected at 1.75 Å in BCl_3 (ref. 62) and 1.90 Å in BBr_3,[63] are not observed, indicating that boron atoms primarily bond with oxygen atoms, and that boron–halogen bonds are rare in these glasses. The neutron $S(Q)$ and $T(r)$ for the ^{null}Li glasses were further analysed using the pair function method, with B–O, O–O, and B–B correlations adopted to reproduce the first and second peaks in $T(r)$. The calculated $S(Q)$ and $T(r)$ (black broken curves in Fig. 3(c) and 4(c)) reproduce the experimental data well. The structural parameters derived from the pair function analysis are summarized in Table 4. The B–O coordination number is 3.4 (3.0 + 0.4) in all the glasses, indicating that the network consists primarily of triangular BO_3 and tetrahedral BO_4 units, consistent with the ^{11}B MAS NMR results (Fig. S2 and Table S2). The structural parameters for the O–O and B–B correlations are comparable to those in B_2O_3 (Table S1) and $LiBO_2$ (Table 3) glasses. It should be noted that lithium–halogen correlations overlap with other peaks in all the $T(r)$ data, making it difficult to extract precise lithium–halogen coordination numbers. Therefore, although the presence of lithium–halogen correlations is suggested, their coordination numbers cannot be reliably determined from conventional diffraction measurements.

3.4 Lithium-specific coordination number analyses using NDIS data

To obtain Li-specific structural information, $\Delta_{Li}S(Q)$ for the Cl100, Cl50Br50, and Br100 glasses were analysed (Fig. 5(a)). These data were obtained by taking the difference between the neutron diffraction data of the ^{nat}Li and ^{null}Li glasses. A negative peak is observed at $Q \sim 2$ Å^{-1} in all the glasses. Majérus *et al.* reported that a similar negative peak originates from Li-centred intermediate-range ordering in Li_2O–$2B_2O_3$ glass.[40] However, in the present $1/3Li_2O$–$1/3B_2O_3$–$1/3LiCl_{1-x}Br_x$ glasses, the peak appears at a higher Q position and exhibits an asymmetric shape, suggesting the formation of a Li-centred intermediate-range structure with a different characteristic length scale. The differential total correlation functions, $\Delta_{Li}T(r)$, obtained from the Fourier transforms of $\Delta_{Li}S(Q)$ are shown in Fig. 5(b). Three broad peaks arising from Li-related correlations are observed at approximately 1.8–3.0 Å in all the glasses. The first peak at approximately 2.0 Å corresponds to the Li–O correlation, consistent with the negative peak observed in the neutron $T(r)$ data for the ^{nat}Li glasses (Fig. 4(b)). The second peak at approximately 2.4 Å is evident in the Cl100 and Cl50Br50 glasses and is mainly attributed to the Li–Cl correlation, in agreement with the Li–Cl distance (2.45 Å) reported for molten LiCl.[64] In the Br100 glass, the second peak appears as a shoulder peak at approximately 2.5–2.7 Å and is assigned to the Li–Br correlation,

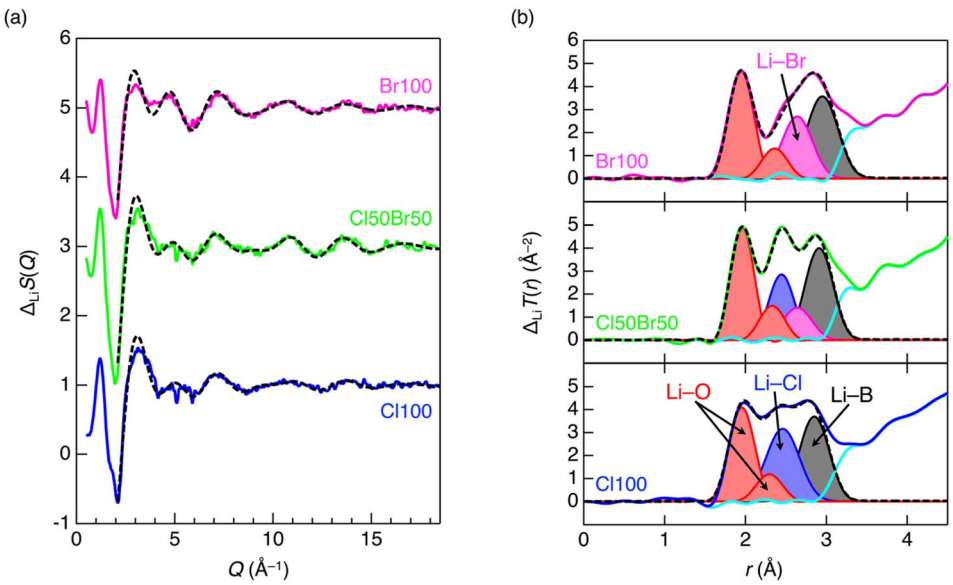

Fig. 5 (a) Differential structure factors and (b) differential total correlation functions of the $1/3Li_2O$–$1/3B_2O_3$–$1/3LiCl_{1-x}Br_x$ glasses. Coloured solid curves and black broken curves represent experimental and calculated data, respectively. The calculated Li–O, Li–Cl, Li–Br, and Li–B correlations are highlighted in red, blue, magenta, and black, respectively, in panel (b). The differences between experimental and calculated data are plotted as cyan curves in panel (b).

Table 5 Structural parameters for Li-related correlations in the $1/3Li_2O–1/3B_2O_3–1/3LiCl_{1-x}Br_x$ glasses, derived from NDIS data

	Li–O (I)		Li–O (II)		Li–Cl		Li–Br		Li–B	
	r_{Li-O} (Å)	N_{Li-O}	r_{Li-O} (Å)	N_{Li-O}	r_{Li-Cl} (Å)	N_{Li-Cl}	r_{Li-Br} (Å)	N_{Li-Br}	r_{Li-B} (Å)	N_{Li-B}
Br100	1.95	2.3	2.36	0.8	—	—	2.64	1.9	2.95	3.0
Cl50Br50	1.96	2.3	2.33	0.9	2.45	1.1	2.64	1.0	2.91	3.1
Cl100	1.96	2.3	2.30	0.8	2.46	1.8	—	—	2.85	3.1

consistent with the Li–Br distance (2.68 Å) in molten LiBr.[64] The third peak mainly originates from the Li–B correlation associated with Li–O–B linkages, as discussed in the X-ray diffraction results for the $LiBO_2$ glasses.

The Li–O, Li–Cl, Li–Br, and Li–B coordination numbers were determined by fitting calculated $\Delta_{Li}S(Q)$ and $\Delta_{Li}T(r)$ to the experimental data using eqn (11). Two Li–O pair functions were adopted based on the results for the $LiBO_2$ glasses. As shown in Fig. 5(a), the calculated $\Delta_{Li}S(Q)$ reproduces the experimental data well for $Q > 2$ Å^{-1}, and good agreement between the calculated and experimental $\Delta_{Li}T(r)$ is also obtained (Fig. 5(b)). The derived structural parameters are summarized in Table 5. The Li–O coordination number is 3.1–3.2 in all the glasses, indicating that the tetrahedral coordination around lithium cations collapses in the halide-containing glasses. Lithium cations are threefold coordinated by oxygen atoms, with two oxygen atoms at approximately 1.95–1.96 Å and one additional oxygen atom at approximately 2.30–2.36 Å, indicating the breaking of one short Li–O bond upon halide addition. The Li–Cl coordination number decreases from 1.8 in the Cl100 glass to 1.1 in the Cl50Br50 (mixed-halide) glass. Similarly, the Li–Br coordination number decreases from 1.9 (Br100) to 1.0 (Cl50Br50). The Li–B coordination number is approximately 3.0 in all the glasses. This behaviour is consistent with the results observed in the $LiBO_2$ glasses, where the Li–B coordination number was almost identical to that of Li–O, suggesting the presence of Li–O–B linkages. To further validate these results, high-energy X-ray diffraction data were analysed based on the NDIS results using the pair-function analysis (eqn (10)). The calculated X-ray $S(Q)$ and $T(r)$ (Fig. S3(a) and (b)) reproduce the experimental data well. The structural parameters for lithium-related correlations derived from the X-ray diffraction data (Tables S3 and S4) agree with those obtained from the NDIS data (Table 5). Additionally, the structural parameters for the B–O, O–O, and B–B correlations also agree with those obtained from the neutron diffraction data of the ^{null}Li glasses (Table 4). These results demonstrate that reliable coordination numbers in the $1/3Li_2O–1/3B_2O_3–1/3LiCl_{1-x}Br_x$ glasses were obtained through an element-specific PDF analysis combining NDIS and high-energy X-ray diffraction data.

3.5 Origin of the improvement in ionic conductivity by mixing of oxide and halide anions

The ionic conductivity of the $1/3Li_2O–1/3B_2O_3–1/3LiCl_{1-x}Br_x$ glasses ($\sim 10^{-6}$ S cm^{-1}) is approximately one order of magnitude higher than that of $LiBO_2$ glass ($\sim 10^{-7}$ S cm^{-1}).[48–50] This enhancement is attributed to the mixing of oxide and halide anions. To clarify the lithium environment responsible for this behaviour, representative lithium–anion polyhedra in $LiBO_2$ and the $1/3Li_2O–1/3B_2O_3–1/3LiCl_{1-x}Br_x$ glasses were visualized based on the coordination number analyses (Fig. 6(a–d)).

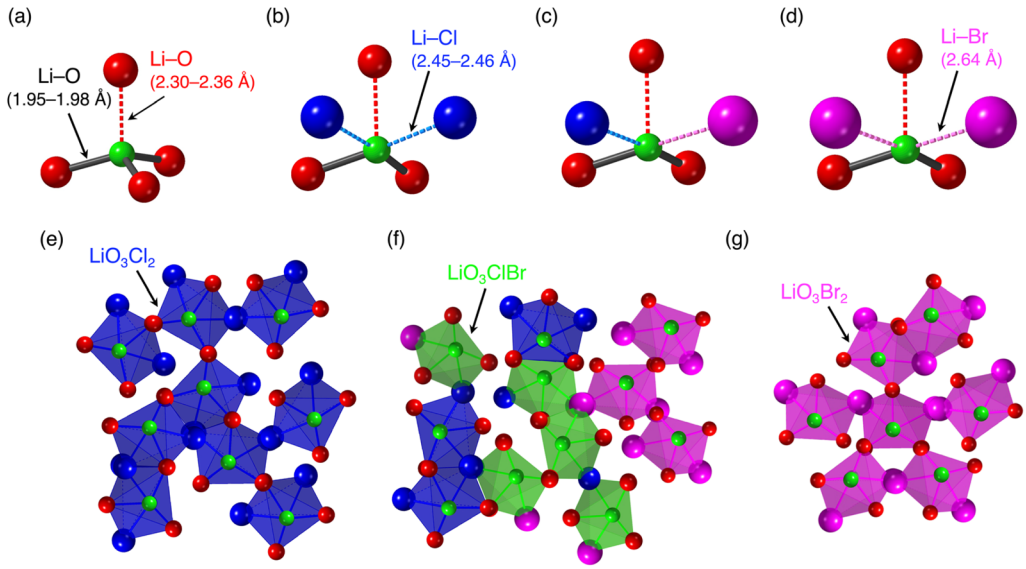

Fig. 6 Schematic representations of typical lithium–anion polyhedra and lithium-ion conduction pathways in $LiBO_2$ and the $1/3Li_2O–1/3B_2O_3–1/3LiCl_{1-x}Br_x$ glasses. (a) LiO_4, (b) LiO_3Cl_2, (c) LiO_3ClBr, and (d) LiO_3Br_2 polyhedra. Lithium-ion conduction pathways formed by lithium–anion polyhedra in (e) Cl100, (f) Cl50Br50, and (g) Br100 glasses. Green: lithium, red: oxygen, blue: chlorine, magenta: bromine.

In $LiBO_2$ glasses, lithium cations are tetrahedrally coordinated by four oxygen atoms: three at 1.98 Å and one at 2.35 Å (Li–O coordination number is 4.1, Table 3) (Fig. 6(a)). Similar tetrahedrally coordinated lithium sites have been reported in binary oxide[39] and sulfide[22,65] glasses, where asymmetric Li–O and Li–S correlation peaks indicate distorted tetrahedra. Upon incorporation of halide anions, the Li–O coordination number decreases from 4.1 to 3.1–3.2 (Table 5). The number of shorter Li–O bonds (1.95–1.98 Å) decreases from 2.9–3.2 to 2.3, whereas the longer Li–O bonds (2.30–2.36 Å) remain nearly unchanged (0.8–1.2). Simultaneously, lithium–halogen coordination numbers of 1.8, 2.1 (1.1 + 1.0), and 1.9 were obtained for the Cl100, Cl50Br50, and Br100 glasses, respectively. These results indicate that lithium cations occupy fivefold-coordinated sites in the halide-containing glasses, denoted as LiO_3X_2 (X = Cl and/or Br) (Fig. 6(b–d)).

The LiO_3Cl_2 (Fig. 6(b)) and LiO_3Br_2 (Fig. 6(d)) units are characteristic of the Cl100 and Br100 glasses, respectively, whereas LiO_3ClBr units (Fig. 6(c)) are additionally present in the mixed-halide Cl50Br50 glass. Similar decreases in Li–O coordination number and the formation of Li–Cl bonds with increasing LiCl content have been reported for $(LiCl)_x(Li_2O–2B_2O_3)_{1-x}$ glasses by neutron diffraction with the aid of RMC modelling.[66] The change in the lithium coordination environments in ternary and quaternary glasses has been observed exclusively through simulation studies; however, the present study directly reveals such changes using Li-specific PDF analysis with NDIS data. The change in lithium coordination numbers plays a pivotal role in enhancing ionic conductivity upon oxide–halide mixing. Incorporation of halide anions replaces one short Li–O bond (1.95–1.98 Å) with two longer Li–halogen bonds (2.45–2.46 Å for Li–Cl; 2.64 Å for Li–Br). According to bond-strength–bond-distance relationships,[67,68] these longer Li–halogen bonds are weaker than Li–O bonds. This is also reflected in bond valence calculations, which relate bond strength to bond length.[69,70] For example, when compared in crystalline lithium oxide (Li_2O) and halides (LiCl and LiBr), the bond valence decreases from 0.236 for Li_2O (Li–O distance: 2.00 Å) to 0.170 for LiCl (Li–Cl distance: 2.565 Å) and 0.141 for LiBr (Li–Br distance: 2.745 Å). Similarly, the single bond strengths calculated from the dissociation energies show that Li–Cl (115 kJ mol^{-1}) and Li–Br (104 kJ mol^{-1})[71] are weaker than Li–O (150 kJ mol^{-1}).[72] Consequently, replacing one short Li–O bond with two longer Li–halogen bonds reduces the local constraints on lithium cations, facilitating lithium-ion migration and enhancing ionic conductivity in the $1/3Li_2O–1/3B_2O_3–1/3LiCl_{1-x}Br_x$ glasses. This interpretation is also consistent with the lower melting points of LiCl (605 °C) and LiBr (552 °C) compared with Li_2O (1570 °C), suggesting that lithium cations bonded to halogens require less thermal energy to become mobile than those bonded to oxygens, despite LiCl or LiBr exhibiting Li–Cl/Br coordination numbers of 6 (higher than the Li–O coordination number of 4 in Li_2O). The specific lithium coordination environments identified in the glasses (Fig. 6(b–d)) are rarely observed in crystalline materials, as the rigid glass network can sustain such metastable structural units.[55,73–75] These unique local structures can provide useful insights into the structural design of glasses with high ionic conductivity.

3.6 Cause of the reduction in ionic conductivity upon mixing of halide anions

Lithium-ion conduction in glasses occurs through pathways formed by interconnected lithium-centred polyhedra.[5,14–17,22,23,66] Therefore, understanding the connectivity of the lithium–oxygen–halogen polyhedra (Fig. 6(b–d)) is essential for elucidating the reduction in ionic conductivity in the $1/3Li_2O–1/3B_2O_3–1/3LiCl_{1-x}Br_x$ glasses caused by halide–halide mixing.

Schematic representations of clusters of LiO_3X_2 units in the Cl100, Cl50Br50, and Br100 glasses are shown in Fig. 6(e–g). In these figures, the network consisting of BO_3 triangles and BO_4 tetrahedra is omitted. In the Cl100 and Br100 glasses, lithium cations predominantly occupy LiO_3Cl_2 (Fig. 6(e)) or LiO_3Br_2 (Fig. 6(g)) polyhedra, forming continuous conduction pathways through fivefold-coordinated sites consisting of three oxide and two halide anions. In contrast, the Cl50Br50 glass contains LiO_3Cl_2, LiO_3Br_2, and LiO_3ClBr units (Fig. 6(f)). The halide-mixed LiO_3ClBr polyhedra create an intermediate local environment with slightly different lithium–halide bond lengths compared with the LiO_3Cl_2 and LiO_3Br_2 units. This structural diversity introduces a mismatch in the occupation energies of the lithium sites, which disrupts lithium-ion migration between different polyhedra. Molecular dynamics simulations of mixed alkali metasilicate glasses have demonstrated that alkali cations migrate along independent pathways and that the ionic conduction among the sites occupied by other types of alkali cations is restricted by energy mismatches.[76,77] Similarly, in the Cl50Br50 glass, the variation in lithium coordination environments leads to a partial inhibition of lithium-ion conduction.

The mixed-halogen effect observed in this study differs from the classical mixed-alkali effect, where conductivity can decrease by several orders of magnitude.[53–55] In the Cl50Br50 glass, the reduction in conductivity is only about half an order of magnitude (Fig. 1), because the substituted halide anions do not act as charge carriers (in contrast to the mixed-alkali effect, where the alkali cations functioning as carriers themselves are substituted). Therefore, the energy mismatch between lithium sites in mixed-halide glasses is smaller than that between different alkali cations in mixed-alkali glasses.

Traditionally, the mixed-anion effect has been associated with the combination of anions with different valences (*e.g.*, oxide and halide), which improves ionic conductivity in glasses.[7,33,34,51,52] However, this study demonstrates that mixing monovalent halides can reduce ionic conductivity. Li-specific PDF analysis combining NDIS data enabled the determination of the lithium-related intermediate-range structure formed by interconnected LiO_3X_2 units. This configuration was identified as the origin of the reduced lithium-ion conductivity in the mixed-halide Cl50Br50 glass.

Anion mixing has a long history in glass science for tuning material properties, and recent studies have extended this strategy to crystalline materials.[78] Well-designed crystalline mixed-anion compounds exhibit unique coordination environments within long-range ordered atomic arrangements and enhanced physicochemical properties, such as pure hydride (H^-) conduction in $La_{2-x-y}Sr_{x+y}LiH_{1-x+y}O_{3-y}$ oxyhydrides,[79]

correlated disorder in $SrMO_2N$ (M = Nb, Ta) perovskite oxynitrides,[80] a significant spin–orbit interaction effect in bulk BiTeI,[81] and exceptionally high lithium-ion conductivity in $Li_{9.54}Si_{1.74}P_{1.44}S_{11.7}Cl_{0.3}$ solid electrolyte.[82] Conversely, in glasses, the compositional and structural flexibility allows diverse lithium environments to form, as demonstrated in this study. Although designing new glasses with tailored structures and properties is still challenging, the insights from element-specific quantum-beam analyses, as demonstrated in this study, pave the way for future glass design.

4. Conclusions

In this study, we investigated the lithium-cation environment in $1/3Li_2O$–$1/3B_2O_3$–$1/3LiCl_{1-x}Br_x$ glasses, which exhibit variations in ionic conductivity due to anion mixing. We found that oxide–halide mixing enhances ionic conductivity by an order of magnitude compared with $LiBO_2$ glass, whereas halide–halide mixing reduces ionic conductivity to nearly half of the value observed prior to mixing. Lithium-specific coordination number analysis based on neutron diffraction with isotopic substitution for ^{nat}Li- and ^{null}Li-enriched glasses revealed that the conductivity enhancement in oxide–halide mixed glasses arises from the breaking of short lithium–oxygen bonds and the formation of longer lithium–halogen bonds, which weaken constraints on lithium mobility. In a halide–halide mixed glass, analysis of lithium–anion coordination numbers showed the formation of three distinct fivefold lithium–oxygen–halogen polyhedral units. The coexistence of these units forms a polyhedral network that hinders lithium-ion migration due to mismatched site occupation energies. These findings provide new insights into the structure–property relationships of lithium-ion conducting glasses and offer guidance for designing glassy electrolytes with improved ionic conductivity.

Author contributions

Y. O. and Y. T. designed the study. The samples were prepared by H. H. and N. K. Electrical conductivity measurement was performed by N. K. The high-energy X-ray diffraction experiment was conducted by Y. O., Y. T., and S. K. The neutron diffraction experiment was conducted by Y. O., Y. T., and K. I. The obtained data were analysed by Y. O., Y. T., H. H., N. K., M. T. and S. K. Y. O. wrote the manuscript with input from all the authors.

Conflicts of interest

The authors declare that they have no conflict of interest.

Data availability

The data that support the findings of this study are presented in the paper and the supplementary information (SI) file and are available from the corresponding author upon reasonable request. Supplementary information is available. See DOI: https://doi.org/10.1039/d5ta10123a.

Acknowledgements

This work was partially supported by JSPS Grant-in-Aid for Transformative Research Areas (A) "Hyper-Ordered Structures Science" [grant numbers 20H05878 (to S. K.) and 20H05881 (to Y. O. and S. K.)]. The synchrotron radiation experiments were performed at BL04B2 of SPring-8 with the approval of the Japan Synchrotron Radiation Research Institute (JASRI) (Proposal number 2019B1233). The neutron experiments at the Materials and Life Science Facility of J-PARC were performed under a user program (Proposal number 2019B0082).

References

1 T. Minami, Y. Takuma and M. Tanaka, *J. Electrochem. Soc.*, 1977, **124**, 1659–1662.
2 T. Minami, H. Nambu and M. Tanaka, *J. Am. Ceram. Soc.*, 1977, **60**, 467–469.
3 Z. Wang, S. Luo, X. Zhang, S. Guo, P. Li and S. Yan, *J. Non-Cryst. Solids*, 2023, **619**, 122581.
4 Y. Daiko, A. Sakuda, T. Honma and A. Hayashi, *J. Ceram. Soc. Jpn.*, 2022, **130**, 552–557.
5 N. Kamaya, K. Honma, Y. Yamakawa, M. Hirayama, R. Kanno, M. Yonemura, T. Kamiyama, Y. Kato, S. Hama, K. Kawamoto and A. Mitsui, *Nat. Mater.*, 2011, **10**, 682–686.
6 Y. Li, S. Song, H. Kim, K. Nomoto, H. Kim, X. Sun, S. Hori, K. Suzuki, N. Matsui, M. Hirayama, T. Mizoguchi, T. Saito, T. Kamiyama and R. Kanno, *Science*, 2023, **381**, 50–53.
7 A. Levasseur, J. C. Brethous, J. M. Reau, P. Hagenmuller and M. Couzi, *Solid State Ionics*, 1980, **1**, 177–186.
8 S. W. Martin and C. A. Angell, *J. Non-Cryst. Solids*, 1986, **83**, 185–207.
9 M. G. Moustafa, K. M. A. Saron, M. Saad, M. S. Alqahtani, A. Qasem and A. S. Hassanien, *Solid State Sciences*, 2023, **141**, 107212.
10 S. A. Feller, W. J. Dell and P. J. Bray, *J. Non-Cryst. Solids*, 1982, **51**, 21–30.
11 T. M. Alam and R. K. Brow, *J. Non-Cryst. Solids*, 1998, **223**, 1–20.
12 Y. Waseda, E. Matsubara, K. Sugiyama, I. K. Suh, T. Kawazoe, O. Kasu, M. Ashizuka and E. Ishida, *Sci. Rep. Res. Inst., Tohoku Univ., Ser. A*, 1990, **35**, 19–33.
13 J. Swenson, L. Börjesson and W. S. Howells, *Phys. Rev. B*, 1995, **52**, 9310–9319.
14 J. Swenson, A. Matic, L. Börjesson and W. S. Howells, *Solid State Ionics*, 2000, **136–137**, 1055–1060.
15 J. Swenson and S. Adams, *Phys. Rev. Lett.*, 2003, **90**, 155507.
16 A. Hall, S. Adams and J. Swenson, *Ionics*, 2004, **10**, 396–404.
17 S. Adams and J. Swenson, *J. Phys.: Condens. Matter*, 2005, **17**, S87–S101.
18 A. Hall, S. Adams and J. Swenson, *Phys. Rev. B*, 2006, **74**, 174205.
19 F. Mizuno, A. Hayashi, K. Tadanaga and M. Tatsumisago, *Solid State Ionics*, 2006, **177**, 2721–2725.
20 Y. Seino, M. Nakagawa, M. Senga, H. Higuchi, K. Takada and T. Sasaki, *J. Mater. Chem. A*, 2015, **3**, 2756–2761.

21 M. Murakami, K. Shimoda, S. Shiotani, A. Mitsui, K. Ohara, Y. Onodera, H. Arai, Y. Uchimoto and Z. Ogumi, *J. Phys. Chem. C*, 2015, **119**, 24248–24254.
22 Y. Onodera, K. Mori, T. Otomo, M. Sugiyama and T. Fukunaga, *J. Phys. Soc. Jpn.*, 2012, **81**, 044802.
23 K. Mori, T. Ichida, K. Iwase, T. Otomo, S. Kohara, H. Arai, Y. Uchimoto, Z. Ogumi, Y. Onodera and T. Fukunaga, *Chem. Phys. Lett.*, 2013, **584**, 113–118.
24 K. Ohara, A. Mitsui, M. Mori, Y. Onodera, S. Shiotani, Y. Koyama, Y. Orikasa, M. Murakami, K. Shimoda, K. Mori, T. Fukunaga, H. Arai, Y. Uchimoto and Z. Ogumi, *Sci. Rep.*, 2016, **6**, 21302.
25 T. Ohkubo, K. Ohara and E. Tsuchida, *ACS Appl. Mater. Interfaces*, 2020, **12**, 25736–25747.
26 H. Yamada, K. Ohara, S. Hiroi, A. Sakuda, K. Ikeda, T. Ohkubo, K. Nakata, H. Tsukasaki, H. Nakajima, L. Temleitner, L. Pusztai, S. Ariga, A. Matsuo, J. Ding, T. Nakano, T. Kimura, R. Kobayashi, T. Usuki, S. Tahara, K. Amezawa, Y. Tateyama, S. Mori and A. Hayashi, *Energy Environ. Mater.*, 2024, **7**, e12612.
27 R. K. Guntu, *Mater. Sci. Eng. B*, 2020, **262**, 114784.
28 J. Budida, C. S. Rao, N. R. Chand, R. K. Guntu and N. K. Mohan, *J. Alloy Compd.*, 2025, **1037**, 182433.
29 G. R. Kumar, M. K. Rao, T. Srikumar, M. C. Rao, V. R. Kumar, N. Veeraiah and C. S. Rao, *J. Alloy Compd.*, 2018, **752**, 179–190.
30 R. K. Guntu, V. Venkatramu, C. S. Rao and V. R. Kumar, *Opt. Mater.*, 2021, **113**, 110876.
31 R. K. Guntu, *Ceram. Int.*, 2025, **51**, 16524–16538.
32 P. Zhang, C. Calahoo, J. Cao, A. Duval and L. Wondraczek, *Glass Europe*, 2025, **3**, 125–146.
33 B. Carette, M. Ribes and J. L. Souquet, *Solid State Ionics*, 1983, **9–10**, 735–738.
34 M. Tatsumisago, N. Machida and T. Minami, *J. Ceram. Assoc. Jpn.*, 1987, **95**, 197–201.
35 V. F. Sears, Neutron Scattering, Part A, in *Methods of Experimental Physics*, ed. K. Sköld and D. L. Price, Academic Press, 1986, vol. 23, pp. 521–550.
36 S. Biggin and J. E. Enderby, *J. Phys. C: Solid State Phys.*, 1981, **14**, 3129–3136.
37 I. Petri, P. S. Salmon and H. E. Fischer, *Phys. Rev. Lett.*, 2000, **84**, 2413–2416.
38 P. S. Salmon and I. Petri, *J. Phys.: Condens. Matter*, 2003, **15**, S1509–S1528.
39 J. Zhao, P. H. Gaskell, M. M. Cluckie and A. K. Soper, *J. Non-Cryst. Solids*, 1998, **232–234**, 721–727.
40 O. Majérus, L. Cormier, G. Calas and A. K. Soper, *Phy. B*, 2004, **350**, 258–261.
41 L. Cormier, P. H. Gaskell, G. Calas, J. Zhao and A. K. Soper, *Phys. Rev. B*, 1998, **57**, R8067–R8070.
42 K. Ohara, Y. Onodera, M. Murakami and S. Kohara, *J. Phys.: Condens. Matter*, 2021, **33**, 383001.
43 S. Kohara, M. Itou, K. Suzuya, Y. Inamura, Y. Sakurai, Y. Ohishi and M. Takata, *J. Phys.: Condens. Matter*, 2007, **19**, 506101.
44 T. Otomo, K. Suzuya, M. Misawa, N. Kaneko, H. Ohshita, T. Fukunaga, K. Itoh, K. Mori, M. Sugiyama, M. Kameda, Y. T. Yamaguchi, K. Yoshida, Y. Kawakita, K. Maruyama, S. Shamoto, S. Takeda, S. Saitoh, S. Muto, J. Suzuki, I. Ino, H. Shimizu, T. Kamiyama, S. Ikeda, Y. Yasu, K. Nakayoshi, H. Senda, S. Uno and M. Tanaka, *KENS Rep.*, 2011, **17**, 28–36.
45 T. E. Faber and J. M. Ziman, *Phil. Mag.*, 1965, **11**, 153–173.
46 E. Lorch, *J. Phys. C: Solid State Phys.*, 1969, **2**, 229–237.
47 R. L. Mozzi and B. E. Warren, *J. Appl. Cryst.*, 1969, **2**, 164–172.
48 M. Tatsumisago, K. Yoneda, N. Machida and T. Minami, *J. Non-Cryst. Solids*, 1987, **95–96**, 857–864.
49 N. Tsuda, M. Tanida and T. Miyajima, *AGC Res. Rep.*, 2018, **68**, 8–12.
50 V. Montouillout, H. Fan, L. del Campo, S. Ory, A. Rakhmatullin, F. Fayon and M. Malki, *J. Non-Cryst. Solids*, 2018, **484**, 57–64.
51 S. W. Martin, *J. Am. Ceram. Soc.*, 1991, **74**, 1767–1783.
52 H. Wada, M. Menetrier, A. Levasseur and P. Hagenmuller, *Mater. Res. Bull.*, 1983, **18**, 189–193.
53 J. O. Isard, *J. Non-Cryst. Solids*, 1969, **1**, 235–261.
54 M. Tomozawa and V. McGahay, *J. Non-Cryst. Solids*, 1991, **128**, 48–56.
55 Y. Onodera, Y. Takimoto, H. Hijiya, T. Taniguchi, S. Urata, S. Inaba, S. Fujita, I. Obayashi, Y. Hiraoka and S. Kohara, *NPG Asia Mater.*, 2019, **11**, 75.
56 K. Suzuya, Y. Yoneda, S. Kohara and N. Umesaki, *Phys. Chem. Glasses*, 2000, **41**, 282–285.
57 R. L. Mozzi and B. E. Warren, *J. Appl. Cryst.*, 1970, **3**, 251–257.
58 A. C. Hannon, D. I. Grimley, R. A. Hulme, A. C. Wright and R. N. Sinclair, *J. Non-Cryst. Solids*, 1994, **177**, 299–316.
59 O. L. G. Alderman, C. J. Benmore and J. K. R. Weber, *Appl. Phys. Lett.*, 2020, **117**, 131901.
60 M. Tatsumisago, M. Takahashi, T. Minami, M. Tanaka, N. Umesaki and N. Iwamoto, *J. Ceram. Assoc. Jpn.*, 1986, **94**, 464–469.
61 D. Ravaine, *J. Non-Cryst. Solids*, 1980, **38–39**, 353–358.
62 M. Atoji and W. N. Lipscomb, *J. Chem. Phys.*, 1957, **27**, 195.
63 A. Filipponi and P. D. Angelo, *J. Chem. Phys.*, 1998, **109**, 5356–5362.
64 H. A. Levy, P. A. Agron, M. A. Bredig and M. D. Danford, *Ann. N. Y. Acad. Sci.*, 1960, **79**, 762–780.
65 K. Itoh, M. Sonobe, M. Sugiyama, K. Mori and T. Fukunaga, *J. Non-Cryst. Solids*, 2008, **354**, 150–154.
66 J. Swenson, L. Börjesson and W. S. Howells, *Phys. Rev. B*, 1998, **57**, 13514–13526.
67 I. D. Brown and R. D. Shannon, *Acta. Cryst.*, 1973, **A29**, 266–282.
68 R. D. Shannon, *Acta. Cryst.*, 1976, **A32**, 751–767.
69 I. D. Brown and D. Altermatt, *Acta Cryst.*, 1985, **B41**, 244–247.
70 I. D. Brown, *Chem. Rev.*, 2009, **109**, 6858–6919.
71 P. Cortona, *Phys. Rev. B*, 1992, **46**, 2008–2014.
72 K.-H. Sun, *J. Am. Ceram. Soc.*, 1947, **30**, 277–281.
73 S. Kohara, K. Suzuya, K. Takeuchi, C. -K Loong, M. Grimsditch, J. K. R. Weber, J. A. Tangeman and T. S. Key, *Science*, 2004, **303**, 1649–1652.
74 Y. Onodera, S. Kohara, H. Masai, A. Koreeda, S. Okumura and T. Ohkubo, *Nat. Commun.*, 2017, **8**, 15449.
75 T. Aoyagi, S. Kohara, T. Naito, Y. Onodera, M. Kodama, T. Onodera, D. Takamatsu, S. Tahara, O. Sakata, T. Miyake,

K. Suzuya, K. Ohara, T. Usuki, Y. Hayashi and H. Takizawa, *Sci. Rep.*, 2020, **10**, 7178.

76 J. Habasaki, I. Okada and Y. Hiwatari, *J. Non-Cryst. Solids*, 1995, **183**, 12–21.

77 J. Habasaki, I. Okada and Y. Hiwatari, *J. Non-Cryst. Solids*, 1996, **208**, 181–190.

78 H. Kageyama, K. Hayashi, K. Maeda, J. P. Attfield, Z. Hiroi, J. M. Rondinelli and K. R. Poeppelmeier, *Nat. Commun.*, 2018, **9**, 772.

79 G. Kobayashi, Y. Hinuma, S. Matsuoka, A. Watanabe, M. Iqbal, M. Hirayama, M. Yonemura, T. Kamiyama, I. Tanaka and R. Kanno, *Science*, 2016, **351**, 1314–1317.

80 M. Yang, J. Oró-Solé, J. A. Rodgers, A. B. Jorge, A. Fuertes and J. P. Attfield, *Nat. Chem.*, 2011, **3**, 47–52.

81 K. Ishizuka, M. S. Bahramy, H. Murakawa, M. Sakano, T. Shimojima, T. Sonobe, K. Koizumi, S. Shin, H. Miyahara, A. Kimura, K. Miyamoto, T. Okuda, H. Namatame, M. Taniguchi, R. Arita, N. Nagaosa, K. Kobayashi, Y. Murakami, R. Kumai, Y. Kaneko, Y. Onose and Y. Tokura, *Nat. Mater.*, 2011, **10**, 521–526.

82 Y. Kato, S. Hori, T. Saito, K. Suzuki, M. Hirayama, A. Mitsui, M. Yonemura, H. Iba and R. Kanno, *Nat. Energy*, 2016, **1**, 16030.

